Frontiers of Physics
https://doi.org/10.1007/s11467-021-1060-2
Front. Phys.
16(4), 43504 (2021)

RESEARCH ARTICLE

Surface plasmon resonance and field confinement in graphene nanoribbons in a nanocavity

Sa Yang†, Ren-Long Zhou‡, Yang-Jun Huang

School of Physics and Information Engineering, Guangdong University of Education, Guangzhou 510303, China
Corresponding authors. E-mail: †yangsa@gdei.edu.cn, †rlzhoupc@sina.com
Received October 27, 2020; accepted January 20, 2021

In this work, we demonstrate surface plasmon resonance properties and field confinement under a strong interaction between a waveguide and graphene nanoribbons (GNRs), obtained by coupling with a nanocavity. The optical transmission of a waveguide–cavity–graphene structure is investigated by finite-difference time-domain simulations and coupled-mode theory. The resonant frequency and intensity of the GNR resonant modes can be precisely controlled by tuning the Fermi energy and carrier mobility of the graphene, respectively. Moreover, the refractive index of the cavity core, the susceptibility $\chi^{(3)}$ and the intensity of incident light have little effect on the GNR resonant modes, but have good tunability to the cavity resonant mode. The cavity length also has good tunability to the resonant mode of cavity. A strong interaction between the GNR resonant modes and the cavity resonant mode appears at a cavity length of $L_1 = 350$ nm. We also demonstrate the slow-light effect of this waveguide–cavity–graphene structure and an optical bistability effect in the plasmonic cavity mode by changing the intensity of the incident light. This waveguide–cavity–graphene structure can potentially be utilised to enhance optical confinement in graphene nano-integrated circuits for optical processing applications.

Keywords graphene nanoribbon, surface plasmon resonance, confinement

1 Introduction

Graphene has received substantial attention in the fields of carbon-based nanomaterials and optoelectonic devices due to its remarkable electronic, mechanical and optical properties, including dynamic tunability, extreme confinement and low losses [1]. Surface plasmon resonance (SPR) plays a critical role in the properties of graphene and has numerous applications in optical devices such as band-pass filters, optical waveguides, infrared detector focal plane arrays, directional couplers and metal–dielectric–metal waveguides [2–4]. Compared with traditional plasmonic materials, plasmons in graphene, as a new plasmonic material, exhibit many unusual behaviours, including a higher wave velocity, longer lifetime and longer propagation distance [5]. The frequency tunability based on electrostatic gating or Fermi energy is an important characteristic of graphene plasmons (GPs) [6].

Graphene nanoribbons (GNRs) can directly couple propagating electromagnetic waves into bound collective charge oscillations [7]. However, the absorption of highly confined plasmonic waves in monolayer graphene is ~2.3% [8, 9]. Therefore, methods for enhancing the absorption in graphene plasmonic devices have been investigated [10–12]. GPs have been studied in a variety of patterns, such as disc, ring, nanoribbon and antidote array patterns [13–16]. Multiple coupling systems have been demonstrated, including band-pass filters, optical splitters, all-optical switches, graphene gratings and directional couplers [17, 18]. Numerous graphene structures have been designed to obtain surface plasmons and to improve the confinement in graphene. Previous works in graphene have demonstrated that GPs have a better tunability and lower loss than plasmons in metals. High absorption has been reported in grating-coupled graphene embedded in a Fabry–Perot cavity [19]. Additionally, GNR arrays have stronger coupling than single GNRs [20, 21]. Such designs also have advantages such as ease in fabrication, strong localization and zero bending loss [22]. Plasmonic–photonic absorption properties and their ultrafast dynamics in two-dimensional (2D) materials have broad applications for photodetectors [23–25], quantum dots [26–28], saturable absorbers [29, 30], biomedical devices [31–33], photothermal devices [34–36] and other 2D material nanoplatforms [37–43]. The limitations in controllable tuning between a single GNR and a propagating wave hinder the development of graphene

*Special Topic: Black Phosphorus and Its Analogues (Eds. Xianhui Chen, Haibo Zeng, Han Zhang & Yuanbo Zhang). This article can also be found at http://journal.hep.com.cn/fop/EN/10.1007/s11467-021-1060-2.

plasmonic devices. Moreover, there are few reports of enhanced absorption in a single finite GNR. However, layered graphene systems and GNRs have exhibited the ability to directly tune plasmons in nanostructures, such as sinusoidally curved and planar graphene layer systems [44], double-layered GNR systems [45] and GNRs coupled with dielectric grating loaded graphene layer resonators [46].

This paper presents optical confinement in two GNR layers combined with a plasmonic cavity and a waveguide based on the finite-difference time-domain (FDTD) method. In addition to the FDTD approach, the rapid and reliable temporal coupled-mode theory (CMT) method [47, 48] is also used to analyse this plasmonic waveguide–cavity–graphene (WCG) structure. The plasmonic WCG structure can couple the electromagnetic field of the plasmonic waveguide into a cavity resonator and the GNRs. The two GNR layers play an important role in tuning the plasmons in the GNRs and the cavity. Furthermore, the three resonant modes in this system are investigated separately by altering the Fermi energy of the GNRs, the carrier mobility of the GNRs, the cavity length, the refractive index of the cavity core, the susceptibility $\chi^{(3)}$ and the intensity of the incident light. We also present the slow-light effect of this WCG structure and an optical bistability effect in the plasmonic cavity mode by changing the intensity of the incident light. The designed WCG structure can be potentially applied to optical confinement in integrated circuits for optoelectronic processing.

2 Design of the structure model

Figure 1 shows a schematic of the WCG structure, which consists of a plasmonic waveguide, a cavity resonator and two GNRs. A plane wave with a polarised E_x component is emitted from the left port of the plasmonic waveguide and propagates along the x-axis direction. To model the transmission and absorption properties of the structure, the perfectly matched layer (PML) absorbing boundary condition is employed.

The cavity resonator has a length of $L_1 = 400$ nm and a width of $L_2 = 300$ nm. One GNR, G_1, with length L_1 is placed in the cavity at a distance of $h_1 = 170$ nm from the bottom of the cavity along the y direction. Another GNR, G_0, with the same length L_1 is also placed in the cavity at a distance of $h_2 = 150$ nm from the bottom of the cavity. The distance between G_0 and G_1 is 20 nm. The metal in our structure is silver, which can be defined by the Drude model: $\varepsilon_m(\omega) = \varepsilon_\infty - \omega_p^2/\omega\,(\omega + \mathrm{i}\gamma)$ [22]. Here the dielectric constant at infinite frequency ε_∞, the plasma frequency ω_p and the damping rate γ are set as 3.7, 1.38 $\times 10^{16}$ rad/s and 2.73 $\times 10^{13}$ rad/s, respectively. We assume that the dielectric in the waveguide is air and set the waveguide width as 100 nm. The coupling thickness h_3 between the waveguide and cavity resonator is 20 nm.

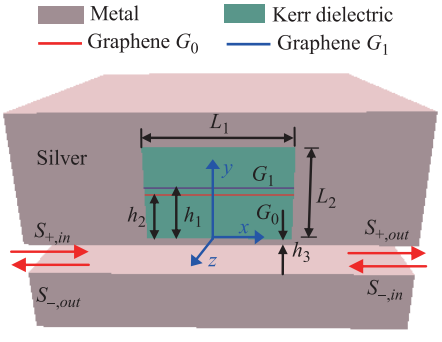

Fig. 1 Schematic of the plasmonic WCG structure.

At room temperature, the intraband conductivity σ_{intra} of graphene is given by $\sigma_{intra} = -\mathrm{i}e^2E_f/[\pi\hbar^2(\omega - \mathrm{i}\tau^{-1})]$ [21], where $\hbar$, e, τ and E_f denote the reduced Planck constant, electric charge, carrier relaxation time and Fermi energy, respectively. The relaxation time τ can be determined by the carrier mobility μ and Fermi energy E_f in graphene as $\tau = (\mu E_f)/(ev_f^2)$. The carrier mobility μ is 1 m^2/(V·s), and the Fermi velocity v_f is ~10^6 m/s. The Fermi energy in G_0 is fixed at $E_f = 0.64$ eV in this paper, and the Fermi energy in G_1 is noted as E_{f,G_1}. Both G_0 and G_1 have a thickness of $h = 1$ nm. The graphene exhibits a metal-like response to an in-plane electric field and a dielectric-like response to a surface-normal electric field. The in-plane dielectric tensor component is $\varepsilon_{11} = \varepsilon_{33} = 1 + \mathrm{i}\sigma_{intra}/(\varepsilon_0\omega h)$, and the surface-normal dielectric tensor component is $\varepsilon_{22} = 1$.

A third-order nonlinear dielectric material is used to fill the cavity, with a dielectric constant of ε_d. Under nonlinear conditions, the dielectric constant ε_d of the Kerr material depends on the intensity of the electric field $|E|^2$ as $\varepsilon_d = \varepsilon_0 + \chi^{(3)}\,|E|^2$, where the linear refractive index ε_0 is set to 1.0 and the third-order nonlinear susceptibility is set to $\chi^{(3)} = 1 \times 10^{-14}$ m^2/V^2.

For the WCG structure, the dynamic transmission features can be analysed by the CMT. $S_{\pm,in}$ and $S_{\pm,out}$ denote the incoming and outgoing waves in the waveguide ports, and the subscript $\pm$ represents the two propagating directions of the waveguide modes. The transfer function $t(\omega) = S_{\pm,out}/S_{\pm,in}$ of this plasmonic WCG system can be calculated by the following formula:

$$t(\omega) = 1 - \left(\sqrt{\frac{1}{\tau_{w1}}} + \sqrt{\frac{1}{\tau_{i1}}}\right)P_0P_1 - \left(\sqrt{\frac{1}{\tau_{w2}}} + \sqrt{\frac{1}{\tau_{i2}}}\right)P_0P_2 - \left(\sqrt{\frac{1}{\tau_{w3}}} + \sqrt{\frac{1}{\tau_{i3}}}\right)P_0P_3, \quad (1)$$

$$P_0 = (\chi_1\chi_4\chi_5 + \chi_1\chi_3\gamma_3 + \chi_2\chi_5\gamma_2 + \chi_2\chi_3\chi_6 + \gamma_1\chi_4\chi_6 - \gamma_1\gamma_2\gamma_3)^{-1}, \quad (2)$$

$$P_1 = (\gamma_2\gamma_3 - \chi_4\chi_6)\sqrt{\frac{1}{\tau_{w1}}} + (\chi_1\gamma_3 + \chi_2\chi_6)\sqrt{\frac{1}{\tau_{w2}}} + (\chi_2\gamma_2 + \chi_1\chi_4)\sqrt{\frac{1}{\tau_{w3}}}, \quad (3)$$

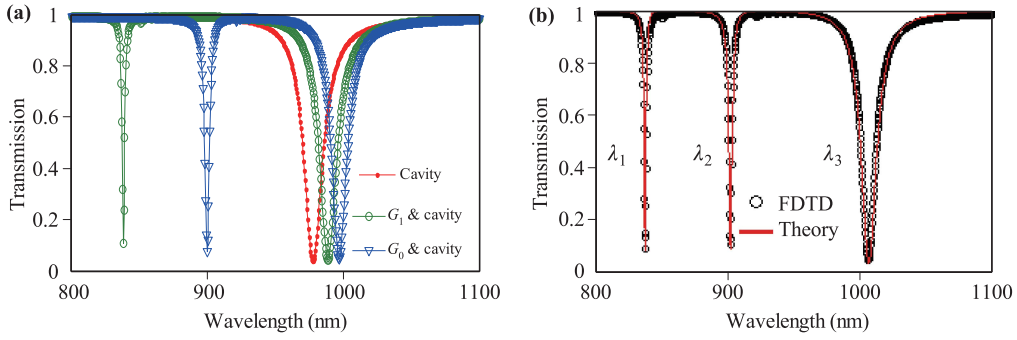

Fig. 2 **(a)** Transmission spectrum for the cavity only (red line), G_0 and the cavity (blue line), and G_1 and the cavity (green line) existing in the WCG structure based on FDTD simulations. **(b)** Transmission spectra based on FDTD simulations (black circles) and the CMT (red line) for the cavity and two GNRs existing in the WCG structure.

$$P_2 = (\chi_4\chi_5 + \chi_3\gamma_3)\sqrt{\frac{1}{\tau_{w1}}} + (\gamma_1\gamma_3 - \chi_2\chi_5)\sqrt{\frac{1}{\tau_{w2}}} + (\gamma_1\chi_4 + \chi_2\chi_3)\sqrt{\frac{1}{\tau_{w3}}}, \quad (4)$$

$$P_3 = (\gamma_2\chi_5 + \chi_3\chi_6)\sqrt{\frac{1}{\tau_{w1}}} + (\gamma_1\chi_6 + \chi_1\chi_5)\sqrt{\frac{1}{\tau_{w2}}} + (\gamma_1\gamma_2 - \chi_1\chi_3)\sqrt{\frac{1}{\tau_{w3}}}, \quad (5)$$

where $1/\tau_{im}$ $(m = 1, 2, 3)$ is the decay rate due to the intrinsic loss of the m-th mode in the graphene grating and τ_{im} is the lifetime in this process. $1/\tau_{wm}$ is the decay rate due to the energy coupling from each mode into the light field, and τ_{wm} is the lifetime during the process of energy coupling. μ_{ij} $(i, j = 1, 2, 3)$ represents the coefficients of coupling among the three resonant modes. $\omega_m(\lambda_m)$ $(m = 1, 2, 3)$ is the resonant frequency (wavelength) of the three modes. $\delta_m = \omega - \omega_m$, $\gamma_m = \mathrm{i}\delta_m - 1/\tau_{im} - 1/\tau_{wm}$, $\chi_1 = \mathrm{i}\mu_{12}$, $\chi_2 = \mathrm{i}\mu_{13}$, $\chi_3 = \mathrm{i}\mu_{21}$, $\chi_4 = \mathrm{i}\mu_{23}$, $\chi_5 = \mathrm{i}\mu_{31}$, $\chi_6 = \mathrm{i}\mu_{32}$. The transmission of the system can be expressed as $T(\omega) = |t(\omega)|^2$.

3 Surface plasmon resonance and strong field confinement

The FDTD and CMT methods were applied to investigate the optical spectra for this plasmonic WCG structure. The PML boundary conditions enclose the computational domain. The interior of the computational window contains the silver, waveguide, cavity and two GNRs, as shown in Fig. 1. The Fermi energy in G_1 is set as $E_{f,G_1} = 0.74$ eV.

Figure 2 presents transmission spectra for the WCG structure. The red line in Fig. 2(a) shows the transmission spectrum for the cavity only in the WCG structure, in which one transmission dip arises at 977.7 nm. The blue line in Fig. 2(a) shows the transmission spectrum for G_0 and the cavity existing in the WCG structure, in which two transmission dips arise at 900.1 and 997.2 nm. The green line in Fig. 2(a) presents the transmission spectrum for G_1 and the cavity existing in the WCG structure, in which two transmission dips arise at 838.6 and 988.7 nm. Figure 2(b) shows the transmission spectrum for the cavity and two GNRs existing in the WCG structure based on the CMT (red solid line) and numerical FDTD simulations (black circles). Three transmission dips arise, corresponding to resonant wavelengths of $\lambda_1 = 838$ nm, $\lambda_2 = 903$ nm and $\lambda_3 = 1006$ nm, which represent resonant mode 1 of G_1, resonant mode 2 of G_0 and resonant mode 3 of the cavity, respectively. For the results shown in Fig. 2(b), all other CMT parameters were set as follows: $\tau_{w1} = 5.2 \times 10^{12}$ rad/s, $\tau_{w2} = 5.2 \times 10^{12}$ rad/s, $\tau_{w3} = 8.5 \times 10^{12}$ rad/s, $\tau_{i1} = 2.2 \times 10^{12}$ rad/s, $\tau_{i2} = 2.2 \times 10^{12}$ rad/s, $\tau_{i3} = 1.8 \times 10^{12}$ rad/s, $\mu_{12} = \mu_{21} = 2 \times 10^{12}$ rad/s, $\mu_{13} = \mu_{31} = 2 \times 10^{13}$ rad/s, $\mu_{23} = \mu_{32} = 2 \times 10^{13}$ rad/s. Clearly, the FDTD simulation results agree well with the CMT results.

To more clearly illustrate the three resonance modes, the corresponding electric field amplitude distributions ($|E|$) at the transmission dips (λ_1, λ_2 and λ_3) are displayed in Figs. 3(a)–(c). Figures 3(d)–(f) present top view of Figs. 3(a)–(c). It is found that the energy of the electric field at wavelengths λ_1, λ_2 and λ_3 is strongly confined in G_0, G_1 and the cavity, respectively, due to the plasmon resonance effect. Additionally, the intensity of the electric field ($|E|$) in G_0 and G_1 is larger than that in the cavity.

From a practical viewpoint, the ability to tune the spectral response of the GP structure is an essential feature for optical applications. Tunability based on electrostatic gating or Fermi energy is a dominant feature of GPs. The evolution of the transmission spectrum for different Fermi energies E_{f,G_1} with three coupling quality factors ($Q_{12} = 30$, 50 and 200) between G_0 and G_1 were investigated using the CMT, as shown in Fig. 4(a). Figure 4(b) presents a more detailed view of Fig. 4(a). Additional detailed views are also shown in Figs. 4(c)–(f). The transmission spectra (black circles) simulated for four Fermi energies [(c) $E_{f,G_1} = 0.74$ eV, (d) $E_{f,G_1} = 0.64$ eV, (e) $E_{f,G_1} = 0.54$ eV and (f) $E_{f,G_1} = 0.44$ eV] are in good agreement

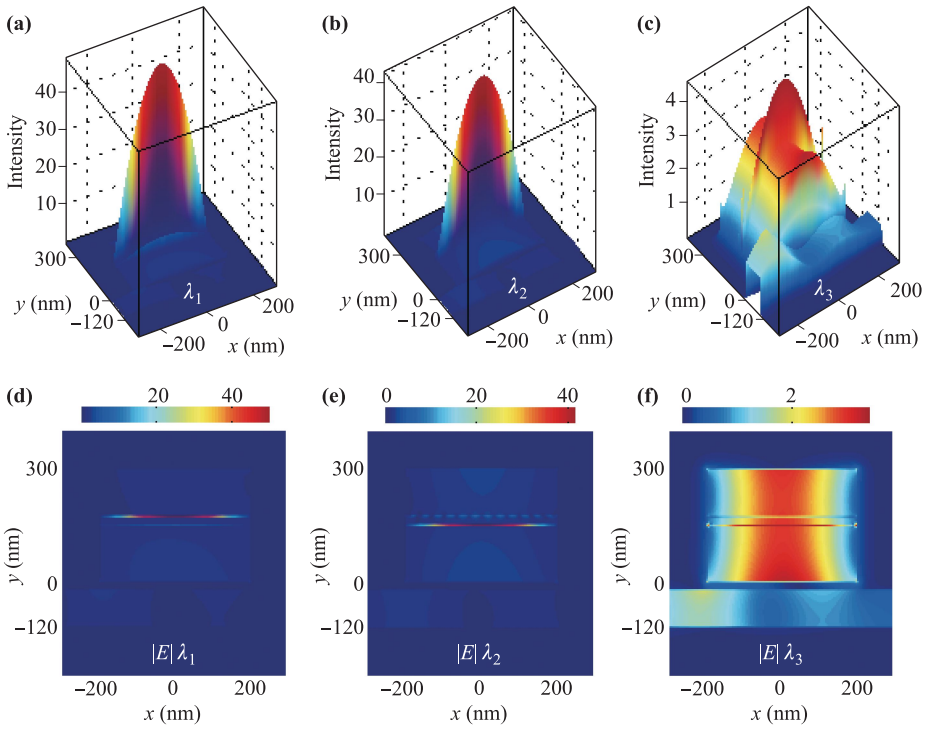

Fig. 3 Electric field amplitude (|E|) distributions of modes 1, 2 and 3 with the corresponding wavelengths: **(a)** λ_1, **(b)** λ_2 and **(c)** λ_3. **(d–f)** present top views of (a), (b) and (c), respectively.

with the CMT results (red line).

Figure 4 shows that graphene plasmon resonant mode 2 remains almost unchanged at $\lambda_2 = 903$ nm when E_{f,G_0} is fixed at 0.64 eV. Meanwhile, graphene plasmon resonant mode 1 can be tuned by altering E_{f,G_1}. This structure exhibits strong localisation in the two GNRs due to the enhanced interaction between the GNRs and the plasmonic waves. Graphene plasmon resonant modes 1 and 2 are denoted as bound states in the continuum (BIC). All of the energy in these modes is confined in the two GNRs. Because of their special properties, BICs are desirable for applications in the design of resonators, lasers, filters and

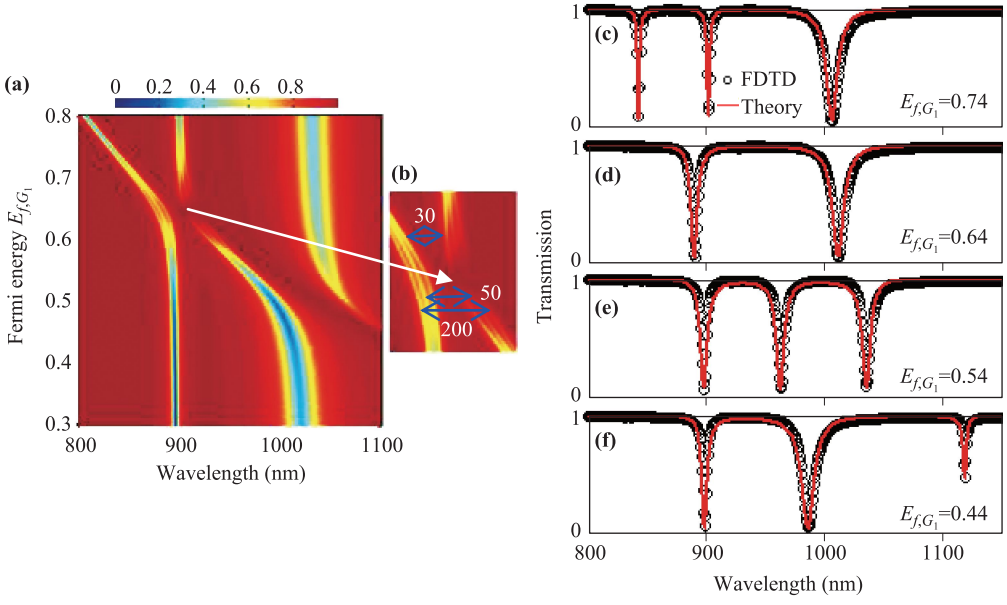

Fig. 4 **(a)** Evolution of transmission based on the CMT for various E_{f,G_1} values with three quality factors Q_{12}. **(b)** A detailed view of the results presented in (a). Transmission for different Fermi energies [**(c)** $E_{f,G_1} = 0.74$ eV, **(d)** $E_{f,G_1} = 0.64$ eV, **(e)** $E_{f,G_1} = 0.54$ eV and **(f)** $E_{f,G_1} = 0.44$ eV] based on the CMT (red line) and FDTD method (black circles).

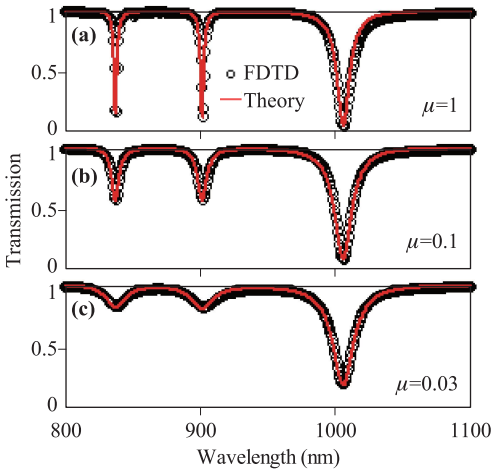

Fig. 5 Transmission spectra for carrier mobilities of **(a)** $\mu = 1\ \mathrm{m^2/(V{\cdot}s)}$, **(b)** $\mu = 0.1\ \mathrm{m^2/(V{\cdot}s)}$ and **(c)** $\mu = 0.03\ \mathrm{m^2/(V{\cdot}s)}$ obtained by the CMT (red line) and the FDTD method (black circles).

biosensors. In Figs. 4(a) and (b), when E_{f,G_1} is equal to 0.64 eV, the graphene plasmon resonant mode 1 of G_1 cannot be excited due to destructive interference from the BIC. Thus, leaky resonance occurs at $E_{f,G_1} = 0.64$ eV. When the Fermi energy E_{f,G_1} in G_1 approaches near 0.64 eV, the resonant frequency of the coupling between G_0 and G_1 can be deduced as $\omega \approx \omega_{\pm} \approx (\omega_1+\omega_2)/2 \pm |\mu_{12}|$. The resonant frequency will split when $\omega_1 \approx \omega_2$. When $\omega_1 \approx \omega_2$, the split frequency difference $\Delta\omega \approx 2\,|\mu_{12}|$ is 5.4314×10^{13} rad/s for $Q_{12} = 200$. Moreover, the split frequency difference $\Delta\omega \approx 2\,|\mu_{12}|$ is $\sim 1.038 \times 10^{14}$ rad/s and 7.7768×10^{13} rad/s for $Q_{12} = 30$ and 50, respectively.

Figure 5 presents transmission spectra for GNRs with different carrier mobilities when E_{f,G_1} is fixed at 0.74 eV. This figure shows that the simulated transmission spectra (black circles) for carrier mobilities of (a) $\mu = 1\ \mathrm{m^2/(V{\cdot}s)}$, (b) $\mu = 0.1\ \mathrm{m^2/(V{\cdot}s)}$ and (c) $\mu = 0.03\ \mathrm{m^2/(V{\cdot}s)}$ are in good agreement with the CMT results (red line). The transmission spectra become broader and shallower as the carrier mobility μ decreases from $\mu = 1\ \mathrm{m^2/(V{\cdot}s)}$ to $\mu = 0.03\ \mathrm{m^2/(V{\cdot}s)}$. Lower carrier mobility in the GNRs corresponds to a higher loss and a lower quality factor. As a result, the interaction between the graphene surface plasmons and waves is reduced, and the binding effect of the graphene plasmon resonance is also reduced. Thus, the intensity of the graphene plasmon resonance can be largely determined by the carrier mobility of the GNRs.

The WCG coupling system also supports low group velocities. The slow-light effect is described by the group index n_g:

$$n_g = \frac{c}{v_g} = \frac{c}{L_1}\tau_g = \frac{c}{L_1}\frac{\mathrm{d}\psi(\omega)}{\mathrm{d}\omega}. \tag{6}$$

Here, v_g denotes the group velocity in the WCG system, τ_g and $\psi(\omega)$ are the optical delay time and transmission phase shift, respectively, and $L_1 = 400$ nm is the length of the cavity in the plasmonic coupled system.

Figure 6(a) shows that the slope of the transmission phase shift is negative and is the steepest at the location of the peaks. The maximum optical delay times τ_g in the transmission are 0.29, 0.23 and 0.27 fs, as shown in Fig. 6(b). A negative optical delay time corresponding to fast light is observed. The group index n_g is depicted in Fig. 6(c). The high group index n_g near the peaks results from strong dispersion. The maximum group index n_g exceeds 0.21 at the peak wavelength, $\lambda_1 = 838$ nm. The slow-light effect of this WCG coupling system can be used in the design of optical storage devices and high-sensitivity sensing devices.

The FDTD method was utilised to investigate the dependence of the transmission characteristics on the length L_1 of the cavity with two GNRs. The parameter E_{f,G_1} was set as $E_{f,G_1} = 0.74$ eV. The evolution of the transmission spectrum with length L_1 in the WCG system without the two GNRs is shown in Fig. 7(a). The results show that the resonance wavelength of the cavity mode varies with length L_1 in an approximately linear manner. Figure 7(b) shows the evolution of the transmission spectrum with length L_1 for the cavity with two GNRs in the WCG structure. When L_1 is less than 380 nm, the GNR resonant modes interact with the cavity resonant mode. A strong interaction occurs when L_1 reaches ~350 nm. As the cavity length changes from 380 to 500 nm, it has little influence on the two GNR resonant modes.

One can also introduce materials that enable the refrac-

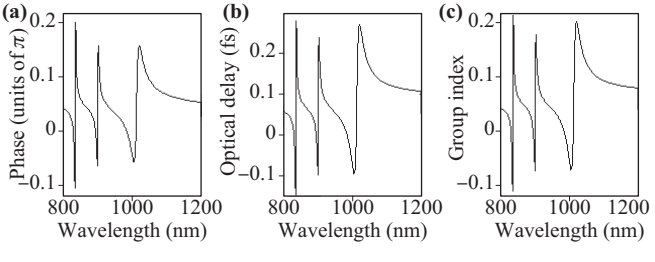

Fig. 6 **(a)** Transmission phase shift, **(b)** optical delay time and **(c)** group index for the WCG coupling system.

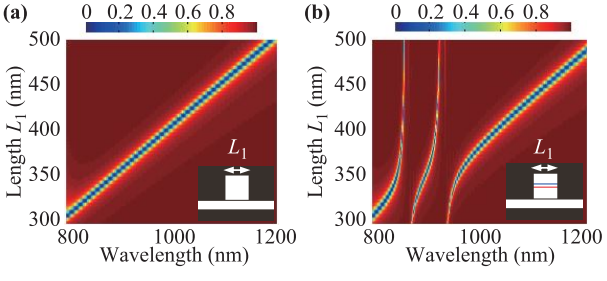

Fig. 7 Evolution of the transmission spectrum for various values of length L_1 **(a)** in a waveguide–cavity structure and **(b)** in the WCG structure.

tive index of the cavity core (n_d) to be changed slightly by external mechanisms such as electro-optic effects. The evolution of the transmission spectrum for different values of n_d is shown in Fig. 8. For a small perturbation of n_d, the results show that one can reliably predict the spectral response for a perturbed cavity resonator. The zero-order cavity mode in line C_1 and the higher-order cavity modes in lines C_2 and C_3 exhibit an approximately linear relation with n_d. Energy splits exist between the second-order modes of the cavity (in line C_3) and modes P_1 and P_2 in the GNRs. The mode 1 of G_1 in line P_1 and the mode 2 of G_0 in line P_2 exhibit little change with n_d.

We also investigated the susceptibility $\chi^{(3)}$ in this system. Figure 9(a) shows the evolution of transmission through the structure for various values of the susceptibility $\chi^{(3)}$. The three resonant wavelengths vary with $\chi^{(3)}$, as shown in Fig. 9(b). Transmission results are shown for three susceptibility values of $\chi^{(3)} = 1$ (red), 0.5 (blue) and 0.01 (black) in Fig. 9(c). For a small value of $\chi^{(3)} = 0.01$, we see three resonant wavelengths of $\lambda_1 = 838$ nm, $\lambda_2 = 903$ nm and $\lambda_3 = 1006$ nm. As $\chi^{(3)}$ increases, the two resonant modes of the two GNRs show little change. However, the resonant wavelength of the cavity mode exhibits a red shift with increasing susceptibility $\chi^{(3)}$.

Figure 10(a) shows the evolution of transmission for various values of the incident light intensity I from $I = 1 \times 10^{10}$ V^2/m^2 to $I = 4 \times 10^{14}$ V^2/m^2. As the intensity of the incident light increases, the two resonant modes of the two GNRs show little change. However, the resonant wavelength of the cavity mode exhibits a red shift as the incident light intensity increases.

From Figs. 8–10, we can see that the refractive index of the cavity core n_d, the susceptibility $\chi^{(3)}$ and the intensity of incident light have little effect on the GNR resonant modes, but can influence the cavity resonant mode. This behaviour is due to the formation of plasmon resonant modes in the GNRs. When light passes through the waveguide, the graphene surface plasmons on the GNRs are excited by a strong interaction among the waveguide, cavity and GNRs. The excited electrons migrate from the metal to the graphene sheet. Subsequently, the GNRs receive excited electrons from the metal, resulting in a collective resonance of a large number of excited electrons. SPR then occurs on the GNR. Thus, the factors that affect the cavity resonant mode, such as n_d, the susceptibility $\chi^{(3)}$ and the intensity of incident light, have little effect on the graphene resonance modes.

To elucidate the bistability behaviour, Fig. 10(b) shows the transmission of the WCG structure as a function of the incident light intensity at a wavelength at 1016 nm. Clearly, significant differences arise in the transmission response as the intensity of the source increases or decreases. A bistability effect is apparent, and the transmission can follow either the upper branch of the bistability loop (corresponding to an increasing source intensity) or the lower branch (corresponding to a decreasing source intensity). As the incident light intensity increases, the transmission decreases rapidly to a value of ~2.7×10^{14} V^2/m^2. Conversely, as the incident light intensity decreases, the trans-

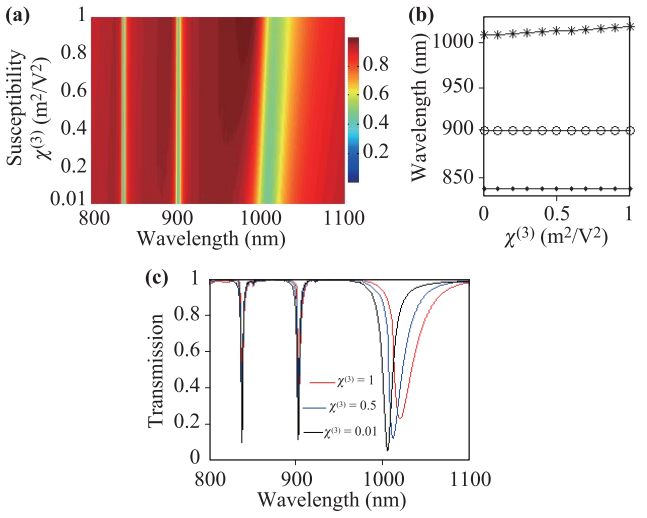

Fig. 9 **(a)** Evolution of transmission for various values of $\chi^{(3)}$. **(b)** Variation in resonant wavelengths with $\chi^{(3)}$. **(c)** Transmission for $\chi^{(3)} = 0.01$ (black), 0.5 (blue) and 1 (red).

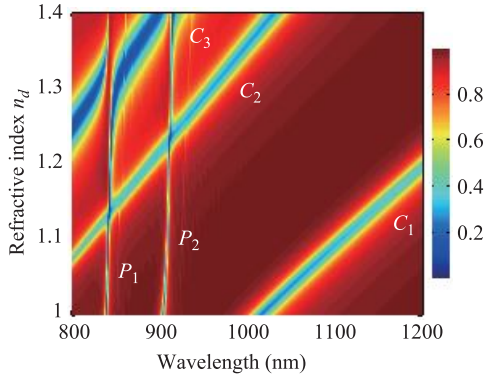

Fig. 8 Evolution of the transmission spectrum for various values of the cavity core refractive index n_d.

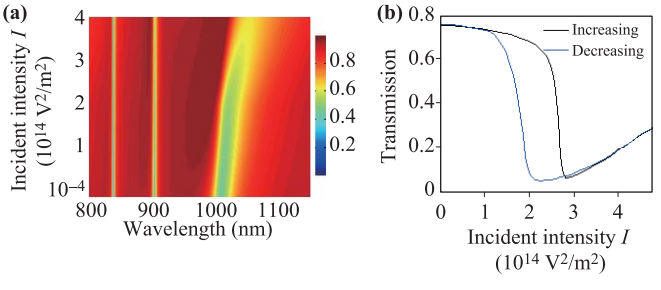

Fig. 10 **(a)** Evolution of transmission for various values of incident light intensity I. **(b)** Optical bistability effect of the mode for a plasmonic cavity at a continuous wavelength of 1016 nm.

mission remains at a lower value and then jumps suddenly to a value of ~1.85 $\times 10^{14}$ V^2/m^2. Thus, this WCG structure can also be used in high-speed optical communication, optical storage, optical limiter and optical logic elements.

4 Conclusions

In conclusion, optical confinement in graphene has been numerically and theoretically studied in a coupling WCG structure by FDTD and CMT methods. The results show that the cavity plays an important role in strengthening the graphene plasmon resonance and boosting confined plasmonic waves in GNRs. Three resonance modes were observed in this WCG system. The resonant frequency and intensity of the GNR resonant modes can be precisely controlled by the Fermi energy and carrier mobility of the graphene, respectively. Although the refractive index of the cavity core, the susceptibility $\chi^{(3)}$ and the intensity of incident light have little effect on the two GNR resonant modes, they can tune the cavity resonant mode. The length of the cavity can also tune the cavity resonant mode. A strong interaction between the GNR resonant modes and the cavity resonant mode appears at a cavity length of $L_1 = 350$ nm. An optical bistability effect was obtained for the plasmonic cavity mode by changing the intensity of the incident light. The proposed configuration and results can provide guidance for further development of optical confinement in graphene devices.

Acknowledgements This work was supported by the Natural Science Foundation of Guangdong Province (No. 2018A030313684) and the Scientific Research Fund of Guangdong Provincial Education Department (Nos. 2019KZDXM061, 2019KQNCX099, and 2020ZDZX2059).

References

1. X. Gan, R. J. Shiue, Y. Gao, I. Meric, T. F. Heinz, K. Shepard, J. Hone, S. Assefa, and D. Englund, Chip-integrated ultrafast graphene photodetector with high responsivity, *Nat. Photon.* 7(11), 883 (2013)
2. J. Liang, W. Hu, Z. Ye, L. Liao, Z. Li, X. Chen, and W. Lu, Improved performance of HgCdTe infrared detector focal plane arrays by modulating light field based on photonic crystal structure, *J. Appl. Phys.* 115(18), 184504 (2014)
3. Y. Gong, L. Wang, X. Hu, X. Li, and X. Liu, Broadbandgap and low-sidelobe surface plasmon polariton reflector with Bragg-grating-based MIM waveguide, *Opt. Express* 17(16), 13727 (2009)
4. J. Miao, W. Hu, Y. Jing, W. Luo, L. Liao, A. Pan, S. Wu, J. Cheng, X. Chen, and W. Lu, Surface plasmon-enhanced photodetection in few-layer MoS_2 phototransistors with au nanostructure arrays, *Small* 11(20), 2392 (2015)
5. H. J. Li, L. L. Wang, B. Sun, Z. R. Huang, and X. Zhai, Tunable mid-infrared plasmonic band-pass filter based on a single graphene ribbon with cavities, *J. Appl. Phys.* 116(22), 224505 (2014)
6. Z. Shi, L. Gan, T. Xiao, H. Guo, and Z. Li, All-optical modulation of a graphene-cladded silicon photonic crystal cavity, *ACS Photon.* 2(11), 1513 (2015)
7. Y. Li, H. Yan, D. B. Farmer, X. Meng, W. Zhu, R. M. Osgood, T. F. Heinz, and P. Avouris, Graphene plasmon enhanced vibrational sensing of surface adsorbed layers, *Nano Lett.* 14(3), 1573 (2014)
8. X. Huang, L. Liu, S. Zhou, and J. Zhao, Physical properties and device applications of graphene oxide, *Front. Phys.* 15(3), 33301 (2020)
9. K. S. Novoselov, D. V. Andreeva, W. Ren, and G. Shan, Graphene and other two-dimensional materials, *Front. Phys.* 14(1), 13301 (2019)
10. Y. Fan, Z. Wei, Z. Zhang, and H. Li, Enhancing infrared extinction and absorption in a monolayer graphene ribbon by harvesting the electric dipolar mode of split ring resonators, *Opt. Lett.* 38(24), 5410 (2013)
11. X. Hu and J. Wang, High-speed gate-tunable terahertz coherent perfect absorption using a split-ring graphene, *Opt. Lett.* 40(23), 5538 (2015)
12. S. Yang, R. Zhou, D. Liu, Q. Lin, and S. Li, Lifetime of enhanced graphene surface plasmon and superstrate sensitivity, *Plasmonics* 15(4), 1103 (2020)
13. Z. Fang, S. Thongrattanasiri, A. Schlather, Z. Liu, L. Ma, Y. Wang, P. M. Ajayan, P. Nordlander, N. J. Halas, and F. J. García de Abajo, Gated tunability and hybridization of localized plasmons in nanostructured graphene, *ACS Nano* 7(3), 2388 (2013)
14. P. Liu, W. Cai, L. L. Wang, X. Zhang, and J. Xu, Tunable terahertz optical antennas based on graphene ring structures, *Appl. Phys. Lett.* 100(15), 153111 (2012)
15. V. V. Popov, T. Y. Bagaeva, T. Otsuji, and V. Ryzhii, Oblique terahertz plasmons in graphene nanoribbon arrays, *Phys. Rev. B* 81(7), 073404 (2010)
16. R. Zhou, S. Yang, D. Liu, and G. Cao, Confined surface plasmon of fundamental wave and second harmonic waves in graphene nanoribbon arrays, *Opt. Express* 25(25), 31478 (2017)
17. B. Wang, X. Zhang, F. J. Garcíavidal, X. Yuan, and J. Teng, Strong coupling of surface plasmon polaritons in monolayer graphene sheet arrays, *Phys. Rev. Lett.* 109(7), 073901 (2012)
18. X. Gan, K. F. Mak, Y. Gao, Y. You, F. Hatami, J. Hone, T. F. Heinz, and D. Englund, Strong enhancement of light-matter interaction in graphene coupled to a photonic crystal nanocavity, *Nano Lett.* 12(11), 5626 (2012)
19. J. Guo, L. M. Wu, X. Y. Dai, Y. J. Xiang, and D. Y. Fan, Absorption enhancement and total absorption in a graphene-waveguide hybrid structure, *AIP Adv.* 7(2), 025101 (2017)
20. T. Xiao, L. Gan, and Z. Li, Graphene surface plasmon polaritons transport on curved substrates, *Photon. Res.* 3(6), 300 (2015)

21. W. Gao, J. Shu, C. Qiu, and Q. Xu, Excitation of plasmonic waves in graphene by guided-mode resonances, *ACS Nano* 6(9), 7806 (2012)
22. H. Lu, X. Liu, D. Mao, and G. Wang, Plasmonic nanosensor based on Fano resonance in waveguide-coupled resonators, *Opt. Lett.* 37(18), 3780 (2012)
23. B. Du, L. Lin, W. Liu, S. Zu, Y. Yu, Z. Li, Y. Kang, H. Peng, X. Zhu, and Z. Fang, Plasmonic hot electron tunneling photodetection in vertical Au-graphene hybrid nanostructure, *Laser Photon. Rev.* 11(1), 1600148 (2017)
24. K. Chen, Y. Wang, J. Liu, J. Kang, Y. Ge, W. Huang, Z. Lin, Z. Guo, Y. Zhang, and H. Zhang, *In situ* preparation of $CsPbBr_3$/black phosphorus heterostructure with optimized interface and photodetector application, *Nanoscale* 11(36), 16852 (2019)
25. B. Wang, S. Zhong, Z. Zhang, Z. Zheng, Y. Zhang, and H. Zhang, Broadband photodetectors based on 2D group IVA metal chalcogenides semiconductors, *Appl. Mater. Today* 15, 115 (2019)
26. H. Shan, Y. Yu, R. Zhang, R. Cheng, D. Zhang, Y. Luo, X. Wang, B. Li, S. Zu, F. Lin, Z. Liu, K. Chang, and Z. Fang, Electron transfer and cascade relaxation dynamics of graphene quantum dots/MoS_2 monolayer mixed-dimensional van der Waals heterostructures, *Mater. Today* 24, 10 (2019)
27. W. Huang, X. Jiang, Y. Wang, F. Zhang, Y. Ge, Y. Zhang, L. Wu, D. Ma, Z. Li, R. Wang, Z. Huang, X. Dai, Y. Xiang, J. Li, and H. Zhang, Two-dimensional beta-lead oxide quantum dots, *Nanoscale* 10(44), 20540 (2018)
28. Y. Ge, W. Huang, F. Yang, J. Liu, C. Wang, Y. Wang, J. Guo, F. Zhang, Y. Song, S. Xu, D. Fan, and H. Zhang, Beta-lead oxide quantum dot (β-PbO QD)/polystyrene (PS) composite films and their applications in ultrafast photonics, *Nanoscale* 11(14), 6828 (2019)
29. C. Ma, C. Wang, B. Gao, J. Adams, G. Wu, and H. Zhang, Recent progress in ultrafast lasers based on 2D materials as a saturable absorber, *Appl. Phys. Rev.* 6(4), 041304 (2019)
30. G. Zhang, X. Tang, X. Fu, W. Chen, B. Shabbir, H. Zhang, Q. Liu, and M. Gong, 2D group-VA fluorinated antimonene: Synthesis and saturable absorption, *Nanoscale* 11(4), 1762 (2019)
31. M. Luo, T. Fan, Y. Zhou, H. Zhang, and L. Mei, 2D black phosphorus-based biomedical applications, *Adv. Funct. Mater.* 29(13), 1808306 (2019)
32. M. Qiu, W. Ren, T. Jeong, M. Won, G. Y. Park, D. K. Sang, L. Liu, H. Zhang, and J. S. Kim, Omnipotent phosphorene: A next-generation, two-dimensional nanoplatform for multidisciplinary biomedical applications, *Chem. Soc. Rev.* 47(15), 5588 (2018)
33. J. Mao, Y. Wang, Z. Zheng, and D. Deng, The rise of two-dimensional MoS_2 for catalysis, *Front. Phys.* 13(4), 138118 (2018)
34. W. Zhang, H. Liu, J. Lu, L. Ni, H. Liu, Q. Li, M. Qiu, B. Xu, T. Lee, Z. Zhao, X. Wang, M. Wang, T. Wang, A. Offenhäusser, D. Mayer, W. T. Hwang, and D. Xiang, Atomic switches of metallic point contacts by plasmonic heating, *Light Sci. Appl.* 8(1), 34 (2019)
35. P. Ghosh, J. Lu, Z. Chen, H. Yang, M. Qiu, and Q. Li, Photothermal-induced nanowelding of metal-semiconductor heterojunction in integrated nanowire units, *Adv. Electron. Mater.* 4(5), 1700614 (2018)
36. D. Li, Y. Gong, Y. Chen, J. Lin, Q. Khan, Y. Zhang, Y. Li, H. Zhang, and H. Xie, Recent progress of two dimensional thermoelectric materials, *Nano-Micro Lett.* 12(1), 36 (2020)
37. D. Ma, J. Zhao, R. Wang, C. Xing, Z. Li, W. Huang, X. Jiang, Z. Guo, Z. Luo, Y. Li, J. Li, S. Luo, Y. Zhang, and H. Zhang, Ultrathin GeSe nanosheets: From systematic synthesis to studies of carrier dynamics and applications for a high-performance UV-Vis photodetector, *Appl. Mater. Interfaces* 11(4), 4278 (2019)
38. M. Zhao, W. Xia, Y. Wang, M. Luo, Z. Tian, Y. Guo, W. Hu, and J. Xue, Nb_2SiTe_4: A stable narrow-gap two-dimensional material with ambipolar transport and mid-infrared response, *ACS Nano* 13(9), 10705 (2019)
39. X. Tang, H. Chen, J. S. Ponraj, S. C. Dhanabalan, Q. Xiao, D. Fan, and H. Zhang, Fluorination-enhanced ambient stability and electronic tolerance of black phosphorus quantum dots, *Adv. Sci.* 5(9), 1800420 (2018)
40. M. Long, Y. Wang, P. Wang, X. Zhou, H. Xia, C. Luo, S. Huang, G. Zhang, H. Yan, Z. Fan, X. Wu, X. Chen, W. Lu, and W. Hu, Palladium diselenide long-wavelength infrared photodetector with high sensitivity and stability, *ACS Nano* 13, 2511 (2019)
41. R. Zhou, J. Peng, S. Yang, D. Liu, Y. Xiao, and G. Cao, Lifetime and nonlinearity of modulated surface plasmon for black phosphorus sensing application, *Nanoscale* 10(39), 18878 (2018)
42. K. Khan, A. K. Tareen, M. Aslam, R. Wang, Y. Zhang, A. Mahmood, Z. Ouyang, H. Zhang, and Z. Guo, Recent developments in emerging two dimensional materials and their applications, *J. Mater. Chem. C* 8(2), 387 (2020)
43. L. Zhang, T. Gong, H. Wang, Z. Guo, and H. Zhang, Memristive devices based on emerging two dimensional materials beyond graphene, *Nanoscale* 11(26), 12413 (2019)
44. S. Xia, X. Zhai, L. Wang, B. Sun, J. Liu, and S. Wen, Dynamically tunable plasmonically induced transparency in sinusoidally curved and planar graphene layers, *Opt. Express* 24(16), 17886 (2016)
45. S. Xia, X. Zhai, L. Wang, and S. Wen, Plasmonically induced transparency in double-layered graphene nanoribbons, *Photon. Res.* 6(7), 692 (2018)
46. J. Guan, S. Xia, Z. Zhang, J. Wu, H. Meng, J. Yue, X. Zhai, L. Wang, and S. Wen, Two switchable plasmonically induced transparency effects in a system with distinct graphene resonators, *Nanoscale Res. Lett.* 15(1), 142 (2020)
47. Q. Li, T. Wang, Y. Su, M. Yan, and M. Qiu, Coupled mode theory analysis of mode-splitting in coupled cavity system, *Opt. Express* 18(8), 8367 (2010)
48. H. Xu, H. Li, B. Li, Z. He, Z. Chen, and M. Zheng, Influential and theoretical analysis of nano-defect in the stub resonator, *Sci. Rep.* 6(1), 30877 (2016)